Hybrid time dependent/independent solution for the He I line ratio temperature and density diagnostic for a thermal helium beam with applications in the scrape-off layer-edge regions in tokamaks

J. M. Muñoz Burgos, O. Schmitz, S. D. Loch, and C. P. Ballance

Citation: Physics of Plasmas **19**, 012501 (2012); doi: 10.1063/1.3672230
View online: https://doi.org/10.1063/1.3672230
View Table of Contents: http://aip.scitation.org/toc/php/19/1
Published by the American Institute of Physics

Hybrid time dependent/independent solution for the He I line ratio temperature and density diagnostic for a thermal helium beam with applications in the scrape-off layer-edge regions in tokamaks

J. M. Muñoz Burgos,[1,a)] O. Schmitz,[2,b)] S. D. Loch,[3,c)] and C. P. Ballance,[3,d)]
[1]*Oak Ridge Institute for Science Education, Oak Ridge, Tennessee 37830, USA*
[2]*Institute für Energieforschung-Plasmaphysik, Forschungszentrum Jülich, Association EURATOM-FZJ, Trilateral Euregio Cluster, D-52425 Jülich, Germany*
[3]*Physics Department, Auburn University, Auburn, Alabama 36849, USA*

(Received 4 August 2011; accepted 2 November 2011; published online 6 January 2012)

Spectroscopic studies of line emission intensities and ratios offer an attractive option in the development of non-invasive plasma diagnostics. Evaluating ratios of selected He I line emission profiles from the singlet and triplet neutral helium spin systems allows for simultaneous measurement of electron density (n_e) and temperature (T_e) profiles. Typically, this powerful diagnostic tool is limited by the relatively long relaxation times of the ^3S metastable term of helium that populates the triplet spin system, and on which electron temperature sensitive lines are based. By developing a time dependent analytical solution, we model the time evolution of the two spin systems. We present a hybrid time dependent/independent line ratio solution that improves the range of application of this diagnostic technique in the scrape-off layer (SOL) and edge plasma regions when comparing it against the current equilibrium line ratio helium model used at TEXTOR. © *2012 American Institute of Physics*. [doi:10.1063/1.3672230]

I. INTRODUCTION

Line intensities and ratios of helium have important applications in determining electron temperatures and densities in laboratory as well as astrophysical plasmas. The application of a stationary (time independent or equilibrium) solution is a standard technique for the quantitative characterization of the plasma edge boundary and the scrape-off layer (SOL) in L-mode plasmas at TEXTOR (Ref. 1) and at PISCES-B.[2]

Helium line intensities and ratios have also been used to provide essential information on the parallel and radial profiles of electron density and temperature both above and at the divertor targets at JET and JT-60U.[3,4] Fast helium beam emission models have been developed and employed at the Madison symmetric torus (MST) for electron temperature and density diagnostic purposes.[5] Efforts for measuring the steep edge electron temperature and density gradients by means of helium line ratios have also been applied at the COMPASS-D tokamak[6] and for edge turbulence measurements in NSTX by gas puff imaging.[7] Helium line ratios are also used in determining 2D electron temperature and density profiles for validation of plasma transport models in MAST.[8] Other efforts include the development of the time dependent collisional radiative numerical code SOPHIA for determination of the neutral helium diffusion coefficients in the edge of magnetically confined plasmas.[9]

Typically, the range of measurements and the accuracy of the helium line ratio technique are limited by the quality of the atomic data employed in the model[8] and the long relaxation times of the triplet spin terms which are populated from the metastable state.[5,10] Here, we report the results of a hybrid time dependent/independent model that overcomes the problem of long relaxation times for the metastable based populations by the implementation of an analytical solution for the time dependent problem. By applying this analytical solution to our diagnostic, we eliminate the need for numerical integration[5] and the use of plasma transport models to predict metastable populations as suggested by Podder *et al.*[10] With this solution, we avoid unphysical high electron temperature measurements in the SOL region that could appear when using equilibrium (stationary) models. This time dependent technique is only necessary for determining a range of lower electron density measurements where the relaxation times for the metastable-triplet system are comparable to the propagation time of a thermal beam. This time dependent solution is then overlapped with an equilibrium (stationary) solution, which is applicable to the higher electron density regimes where the triplet spin system relaxation times are no longer significant compared to the beam propagation time scales. With this technique, we are able to extend the diagnostic out to greater radial distances in the SOL than the model currently employed at TEXTOR.[1]

The successful application of the line ratio technique depends strongly on the accuracy of the set of atomic data used in the solution of the collisional radiative model (CRM).[11] The application of non-perturbative methods like the R-matrix,[12] R-matrix with pseudostates (RMPS),[13] and convergent close coupling (CCC)[14,15] to generate high quality electron-ion collision data has proven to be very reliable. We make the assumption that the main mechanisms for populating/depopulating excited states for a thermal beam

[a)]Electronic mail: munozj@fusion.gat.com.
[b)]Electronic mail: o.schmitz@fz-juelich.de.
[c)]Electronic mail: loch@physics.auburn.edu.
[d)]Electronic mail: ballance@physics.auburn.edu.

(gas puff) in the SOL consist mainly of electron-impact excitation and ionization. Ion-impact excitation and ionization as well as charge exchange become significant for high energy beams only.[16] In order to improve the helium line ratio model, we employ high quality and newly calculated RMPS data from Ballance *et al.*[17] for electron-impact excitation, and RMPS and CCC data for electron impact ionization, which was used for the generation of generalized collisional radiative (GCR) coefficients by Loch *et al.*[18] [which will be soon be made available in the atomic data analysis structure (ADAS)[19] database], and that we used for ionization balance calculations to obtain ionic fractional abundances. These data sets of atomic data were selected not only due to the accuracy of the method employed in their calculations but also due to their high degree of agreement when comparing against experimentally measured atomic collision data.[17]

For comparison, we also generate a generalized CRM by means of the projection matrix from bundle-n onto a resolved nl low term solution.[3,20,21] This method helps us to include contributions from higher Rydberg states by condensing those high terms into the lower and limited N-term model we are using. Muñoz *et al.*[22] have shown that there are significant differences when including the high Rydberg contributions into the helium model when applying the line ratio diagnostic for higher electron temperature-density regions, and which are well within the range of application of the hybrid solution. In this work, we focus on the 667.9 nm, 706.7 nm, and 728.3 nm helium lines in which both 667.9 nm and 728.3 nm get populated primarily from the singlet (^1S) ground term and 706.7 nm from the triplet (^3S) metastable term. Table I shows these lines with their respective transition terms and configurations.

The line ratio between the two singlet based lines proves to be highly sensitive to electron density (667.9 nm/728.3 nm), while the ratios between the triplet and singlet based lines turn out to be more sensitive to temperature (706.7 nm/728.3 nm) and both to temperature and density (706.7 nm/667.9 nm). The sensitivity of the triplet metastable term to electron temperature is a consequence of the high energy difference (19.82 eV) between the triplet metastable term and the singlet ground state. We determine electron temperature and density values from experimentally obtained line emission profiles from TEXTOR.[1] We compare our results obtained from our hybrid model with those obtained with the equilibrium solution applied routinely at TEXTOR. We also compare our results against Thomson and Li beam electron temperature and density experimental profiles. This technique is accurate for localized sources of helium or in regions of uniform electron temperature and density profiles along the line of sight.

TABLE I. Atomic transition terms and configurations.

Spectral line[a] (nm)	Transition term and configuration
667.9	$1s3d(^1D) \rightarrow 1s2p(^1P^o)$
706.7	$1s3s(^3S) \rightarrow 1s2p(^3P^o)$
728.3	$1s3s(^1S) \rightarrow 1s2p(^1P^o)$

[a]Values obtained from NIST (Ref. 23).

This systematic study shows the importance of a time dependent solution not only into line ratio diagnostic applications but also its relevance when modeling neutral beam emission spectroscopy, where the term relaxation times may be comparable to the beam propagation time scales. It also shows the importance of selecting a suitable set of atomic data in the CRM for the successful application of the line ratio diagnostic technique.

II. ATOMIC DATA

The atomic data for neutral helium used in our model consist of electron-impact excitation data calculated using the RMPS method.[17] The calculation is described in detail by Ballance *et al.*,[17] who also showed the importance of including continuum coupling effects in the collision calculation. Ballance *et al.*[17] calculated electron-impact excitation data for electron temperatures ranging from 0.043 to 43.1 eV; we have extended this temperature range to 430.87 eV by means of the high energy Born limit of the collision strength.[25] We apply the Burgess and Tully[25] approach for extending the temperature ranges by means of the ADAS215 code,[19] this more accurate approach gives us very different results for the higher electron temperature regions, than the simple spline extrapolation used by the ADAS208 code we applied for the previous helium line ratio calculation.[22] Electron-impact ionization rate coefficients were taken from CCC calculations.[24] Electron-impact excitation as well as ionization data between all 19 terms in the configurations $1snl$ $(1s < nl < 4f)$ were included.

In the ADAS (Ref. 19) framework, the term-resolved low n-shell atomic data from which one sees the majority of the spectral line emission is supplemented with data for the higher n-shells, in this case up to $n = 500$. The high n-shell effects are projected into the lower N-term populations by means of the projection matrix, which is described in more detail by Summer *et al.*[20] This can often have a significant effect on the N-term populations when applied to high electron temperature and density regimes.[22] There is no direct way to measure experimentally the effects of the high Rydberg effects onto the lower populations; therefore for the sake of comparison, we calculate two data sets where we include the high Rydberg states in one of them. The electron-impact excitation data in the projection matrix consist of semi-empirical Gaunt factor calculations.[26] The electron-impact ionization data from the high n-shells are calculated using the exchange classical impact parameter (ECIP) method.[26] Loch *et al.*[18] found that ECIP cross sections for the ionization of the lower excited states of neutral helium to be more accurate when compared with perturbative calculations; unfortunately, we do not have experimental data to compare the ionization from the ECIP approximation for the higher n-shells of helium. By including the projection matrix in one of our calculations, we construct our comprehensive collisional radiative model that includes the "cascading" effects from populations of higher Rydberg states and compare it against one without these high Rydberg states included.

III. EQUILIBRIUM COLLISIONAL RADIATIVE MODEL

To successfully model spectral emission, it is necessary to account for all the significant populating/depopulating mechanisms in a collisional-radiative model. Our application of collisional-radiative theory to the calculation of excited populations is similar to the concept of the ADAS (Ref. 19) suite of codes for population and emission modeling. Any ion/atom consists of a set of N-terms/levels with radiative and collisional couplings.

The processes that play a role in populating the various ionic term/levels include (but are not limited to)

- Spontaneous decay: $(A_{j\to i}/A_{i\to j})$.
- Electron-impact excitation/de-excitation: $(q^e_{j\to i}/q^e_{i\to j})$.
- Ion-impact excitation/de-excitation: $(q^I_{j\to i}/q^I_{i\to j})$.
- Electron-impact ionization: (S^e_i).
- Ion-impact ionization: (S^I_i).
- Radiative recombination: $[\alpha^{(r)}_i]$.
- Dielectronic recombination: $[\alpha^{(d)}_i]$.
- Three-body recombination: $[\alpha^{(3)}_i]$.
- Charge exchange: (q^{CX}_i).

Figure 1 illustrates some of the processes that may contribute to the population of the ith term, where j represents any higher or lower term from i. In order to compute the excitation and ionization rate coefficients, we have assumed *Maxwellian* distributions for the free electrons.

Any given atom/ion in an arbitrary excited i-term is represented by the following time dependent population equation, with the collisional processes (on the right hand side) included,

$$\begin{aligned}\frac{dn_i}{dt} =& -n_i n_I^{+z} q^{cx}_{i,I} - n_i n_e S^e_i - n_i n_I S^I_i \\ &+ \sum_{j>i}\left(n_j A_{j\to i} + n_j n_e q^e_{j\to i} - n_i n_e q^e_{i\to j} + n_j n_I q^I_{j\to i} - n_i n_I q^I_{i\to j}\right) \\ &+ \sum_{i>j}\left(n_j n_e q^e_{j\to i} - n_i n_e q^e_{i\to j} + n_j n_I q^I_{j\to i} - n_i n_I q^I_{i\to j} - n_i A_{i\to j}\right) \\ &+ n^+ n^{z'}_{I'} q^{cx}_{i,I'} + n^+ n_e \alpha^{(r)}_i + n^+ n_e \alpha^{(d)}_i + n^+ n_e^2 \alpha^{(3)}_i. \end{aligned} \tag{1}$$

Here, n_e represents the free electron density, n_I is the free hydrogenic main ion density, n_i is the population of the ith excited term being described, n_j is the jth population of any higher or lower term from i, n^+ is the free He II density, n_I^{+z} is the free arbitrary ion density that may remove a charge exchange electron from n_i, and $n^{z'}_{I'}$ is another free arbitrary ion density that may contribute an electron by charge exchange to the ith population. These arbitrary ions may represent impurities in the plasma which may be significant if their densities become comparable to the main ion density, and if the beam is energetic enough for charge exchange to become significant. We define our total recombination rate coefficient as $\alpha^R_i = \alpha^{(r)}_i + \alpha^{(d)}_i + n_e\alpha^{(3)}_i$, by regrouping some of the terms in the equation and by changing our notation by setting $A_{i\to j}=0$ for $j>i$, and $q_{i\to j}$ representing electron/ion-impact excitation/de-excitation (depending on the order of the subscripts), we get

$$\begin{aligned}\frac{dn_i}{dt} - n^+[n_e\alpha^R_i + n^{z'}_{I'} q^{cx}_{i,I'}] =& -\left\{n_I^{+z} q^{cx}_{i,I} + n_e S^e_i + n_I S^I_i + \sum_{j\neq i}(A_{i\to j} + n_e q^e_{i\to j} + n_I q^I_{i\to j})\right\} n_i \\ &+ \sum_{j\neq i}(A_{j\to i} + n_e q^e_{j\to i} + n_I q^I_{j\to i}) n_j \end{aligned} \tag{2}$$

or in the more simplified form

$$\frac{dn_i}{dt} = -C_{i,i} n_i + \sum_{j\neq i} C_{i,j} n_j + n^+[n_e\alpha^R_i + n^{z'}_{I'} q^{cx}_{i,I'}], \tag{3}$$

where we have defined a diagonal loss terms of the collisional radiative matrix as

$$C_{i,i} = n_I^{+z} q^{cx}_{i,I} + n_e S^e_i + n_I S^I_i + \sum_{j\neq i}(A_{i\to j} + n_e q^e_{i\to j} + n_I q^I_{i\to j}), \tag{4}$$

and the non-diagonal gain terms of the collisional radiative matrix

$$C_{i,j} = A_{j\to i} + n_e q^e_{j\to i} + n_I q^I_{j\to i}. \tag{5}$$

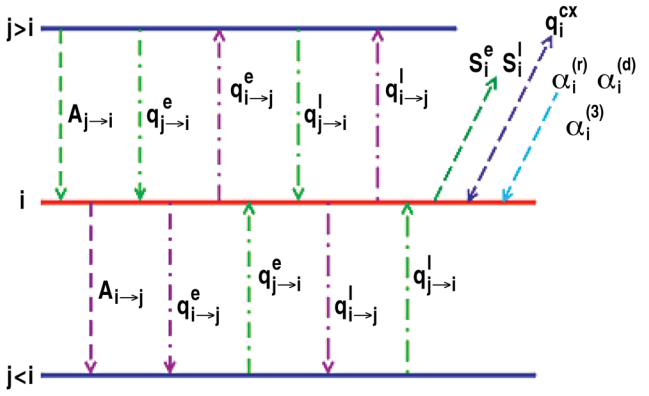

FIG. 1. (Color online) Populating/depopulating atomic processes for the *i*th ionic level/term.

In order to obtain and compare against a comprehensive solution, we account for higher Rydberg states into one of our collisional radiative models. The collisional radiative matrix [Eqs. (4) and (5)] includes only the lower 19 terms or what is defined as the direct part.[20,21] To account for the higher Rydberg contributions or "cascades" into the lower term populations, we make use of the projection matrix that contains the equivalent of these contributions, and in this way build our generalized collisional radiative model by adding the N-term direct contribution C^{dir}_{ij}, with the higher Rydberg contributions or indirect contribution C^{indir}_{ij}.[20,21] Our comprehensive collisional radiative matrix is simply given by

$$C_{i,j} = C^{dir}_{i,j} + C^{indir}_{i,j}. \tag{6}$$

From a total of N terms, we separate the number of metastable terms M (including the ground) and a number of ordinary terms $N-M$, we make this distinction due to the different relaxation times between the two. The time scales for the ordinary terms are so small that it is safe to assume an equilibrium state at all times in comparison to the metastable terms. The relaxation timescale (in seconds) of an excited term, i, may be estimated from[19]

$$\tau_o \sim \frac{1}{\sum_j n_e q^e_{i\to j} + \sum_j A_{i\to j}}. \tag{7}$$

By approximating the dipole transitions by $A_{i\to j} \sim 10^8 (z+1)^4\,\mathrm{s}^{-1}$ (where z is the atomic number[19,27]), we approximate Eq. (7) by[19]

$$\tau_o \sim \frac{10^{-8}}{(z+1)^4}\,\mathrm{s}, \tag{8}$$

which suggests timescales on the order of nanoseconds. Having defined the time scales, we now obtain our equilibrium solution by setting the time derivatives for the ordinary terms in Eq. (3) to zero, this is also known as the quasi-steady-state approximation. Thus, we obtain our equilibrium solution for any of the n_i ordinary term populations in the form

$$n_i = -\sum_{j=1}^{N-M} C^{(r)^{-1}}_{i,j}\left[n^+ n_e \alpha^R_{j+M} + n^+ n^{z'}_{l'} q^{cx}_{j+M,l'} + \sum_{k=1}^{M} n_k C_{j+M,k}\right], \tag{9}$$

where $C^{(r)}_{i,j}$ is the reduced collisional radiative matrix which only includes the ordinary term elements and excludes the metastable terms, and it ends up being a reduced $N-M$ by $N-M$ square matrix with $C^{(r)^{-1}}_{i,j}$ as its inverse. Schmitz *et al.*[1] have shown that ion-impact excitation/ionization processes are negligible for the helium thermal beam case. We, therefore, have neglected any ion-impact interactions and charge exchange in our thermal beam model. In our model, we consider any helium ionization as a loss since the ion gets trapped in the magnetic field lines and gets transported outside the view of the spectrometer. We assume by the time the lost ion recombines with an electron to form again a neutral, it is already far from the view of the spectrometer. We are also neglecting any local recycling that may take place. For these reasons, we have excluded any recombination process in our CRM. We normalize the populations with respect to the ground state ($i=1$), we calculate our normalized populations by setting $n_1 = n^o = 1$, and thus we get $M=1$ since we consider the ground state as our only metastable in the equilibrium model. The final form of our normalized equilibrium population solution is given by

$$\frac{n_i}{n^o} = -\sum_{j=1}^{N-1} C^{(r)^{-1}}_{i,j} C_{j+1,1}. \tag{10}$$

To calculate the line emission [in units of Photons/cm$^2\cdot$s$\cdot$sr] from the $i\to j$ emission line, we use

$$I_{i\to j} = \frac{A_{i\to j}}{4\pi}\int_l n_{He}(\boldsymbol{x})\left[\frac{n^o}{n_{He}}(\boldsymbol{x})\right]\left[\frac{n_i}{n^o}(x)\right]dx, \tag{11}$$

where n_{He} is the total density of neutral helium atoms, n^o/n_{He} is the fractional abundance (or ionization balance) of the total number of atoms in the ground state with respect to the total number of local helium atom/ion density.[19] We account for the total emission by integrating along the line of sight length, this assumes previous knowledge of the $T_e(x)$ and $n_e(x)$ line of sight profiles. Since the gas is being introduced in the form of a collimated beam, we assume the emission to be localized; this assumption makes our profile along the line of sight approximately uniform. Thus, we approximate our local line emission by

$$I_{i\to j} \approx \frac{A_{i\to j}}{4\pi} n_{He}\left[\frac{n^o}{n_{He}}\right]\left[\frac{n_i}{n^o}\right]\Delta x. \tag{12}$$

Therefore, our modeled line ratio is given by the simple expression

$$R^{mod} \approx \frac{A_{i\to j} n_i}{A_{k\to l} n_k}, \tag{13}$$

which we use to calculate our three different ratios for a specific temperature and density grid. We use a range of

electron temperatures from $T_e = 1$ to 200 eV, with resolution of $\Delta T_e = 1$ eV, and a range of electron densities from $n_e = 1.0 \times 10^{10}$ to $1.0 \times 10^{11}\,\mathrm{cm}^{-3}$ with resolution of $\Delta n_e = 1.0 \times 10^{10}\,\mathrm{cm}^{-3}$, and $n_e = 1.0 \times 10^{11}$ to $1.0 \times 10^{13}\,\mathrm{cm}^{-3}$ with resolution of $\Delta n_e = 1.0 \times 10^{11}\,\mathrm{cm}^{-3}$. These electron temperature and density ranges of values have been chosen since they are typically found in the SOL-divertor regions. Figure 2 shows our equilibrium solutions without high Rydberg effects included for the electron temperature sensitive R^{eq}_{Te}(706.7 nm/728.3 nm) and electron density sensitive R^{eq}_{ne}(667.9 nm/728.3 nm) line ratios as a function of electron temperature and density (T_e, n_e). Figure 3 shows our equilibrium solutions with high Rydberg effects included, and Fig. 4 shows the previous modeled results from TEXTOR.[1] For fine-tuning purposes, we have calculated the electron temperature and density sensitive line ratio $R^{eq}_{Te,ne}$(706.7 nm/667.9 nm) as well.

We have defined the following quantity Γ^2 and minimize it to determine our local experimental electron temperature and density values from any experimental line ratio point

$$\Gamma^2(T_e, n_e) = \left[1 - \frac{R^{exp}_{T_e}}{R^{mod}_{T_e}}(T_e, n_e)\right]^2 + \left[1 - \frac{R^{exp}_{n_e}}{R^{mod}_{n_e}}(T_e, n_e)\right]^2 + \left[1 - \frac{R^{exp}_{T_e,n_e}}{R^{mod}_{T_e,n_e}}(T_e, n_e)\right]^2. \quad (14)$$

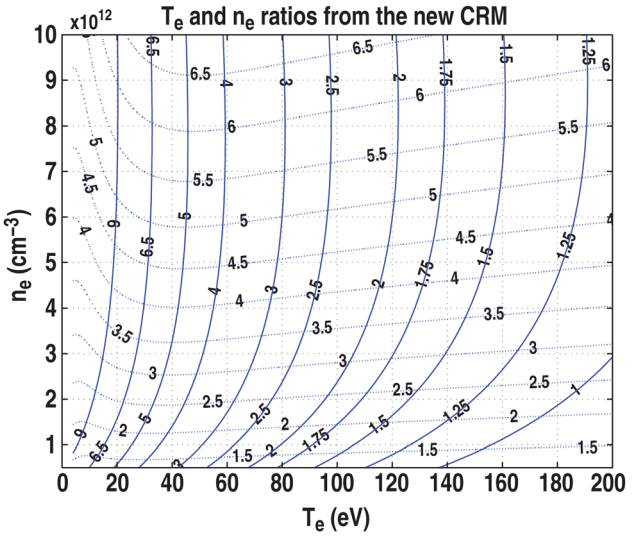

FIG. 2. (Color online) Modeled equilibrium solution without high Rydberg states included, for the electron temperature and density sensitive line ratios. Solid curve represents the calculated value for the 706.7 nm/728.3 nm electron temperature sensitive ratio; dotted curve represents the calculated value for the 667.9 nm/728.3 nm electron density sensitive ratio for our selected electron temperature and density mesh.

IV. TIME DEPENDENT COLLISIONAL RADIATIVE MODEL

Our aim is to develop an analytical time dependent solution which eliminates the need of numerically solving the problem every time the diagnostic is run.[5] Numerical solutions can be time consuming in this case since it would require integrations along a large electron temperature and density range for each one of the experimental points. This could become unpractical when employing this algorithm to process large datasets of experimental data on a shot to shot diagnostic as commonly used in research tokamaks. Our non-equilibrium model is based on analytically solving the simple set of N first order coupled differential equations [Eq. (3)] that conforms to the collisional radiative formalism for a set of different electron temperature and density values. From this solution, we obtain our time dependent line ratios that we use for diagnostic purposes. We start by rewriting Eq. (3) in matrix notation

$$\begin{pmatrix} \frac{dn_1}{dt} \\ \frac{dn_2}{dt} \\ \vdots \\ \frac{dn_N}{dt} \end{pmatrix} = \begin{pmatrix} C_{1,1} & C_{1,2} & \dots & C_{1,N} \\ C_{2,1} & C_{2,2} & \dots & C_{2,N} \\ \vdots & \vdots & \ddots & \vdots \\ C_{N,1} & C_{N,2} & \dots & C_{N,N} \end{pmatrix} \cdot \begin{pmatrix} n_1 \\ n_2 \\ \vdots \\ n_N \end{pmatrix} + \begin{pmatrix} n^+\left[n_e \alpha^R_1 + n^{z'}_{l'} q^{cx}_{1,l'}\right] \\ n^+\left[n_e \alpha^R_2 + n^{z'}_{l'} q^{cx}_{2,l'}\right] \\ \vdots \\ n^+\left[n_e \alpha^R_N + n^{z'}_{l'} q^{cx}_{N,l'}\right] \end{pmatrix} \quad (15)$$

or in vector notation

$$\frac{d\boldsymbol{n}}{dt} = \boldsymbol{C} \cdot \boldsymbol{n} + \boldsymbol{r}. \quad (16)$$

We decouple this set of non-homogeneous linear coupled differential equations by diagonalizing the collisional radiative matrix $\boldsymbol{C}$ [Eq. (6)] by means of the frame transformation $\boldsymbol{n} = \boldsymbol{V} \cdot \boldsymbol{n}'$, where $\boldsymbol{V}$ is the eigenvector matrix obtained from $(\boldsymbol{C} - \boldsymbol{\lambda}) \cdot \boldsymbol{n}' = 0$ and with eigenvalues $|\boldsymbol{C} - \boldsymbol{\lambda}| = 0$. We now express the decoupled solution in the form

$$\frac{d\boldsymbol{n}'}{dt} = \boldsymbol{\lambda} \cdot \boldsymbol{n}' + \boldsymbol{r}', \quad (17)$$

where $\boldsymbol{\lambda} = \boldsymbol{V}^{-1} \cdot \boldsymbol{C} \cdot \boldsymbol{V}$ and $\boldsymbol{r}' = \boldsymbol{V}^{-1} \cdot \boldsymbol{r}$. For any of the k decoupled equations, we get the simple non-homogenious first order differential equation

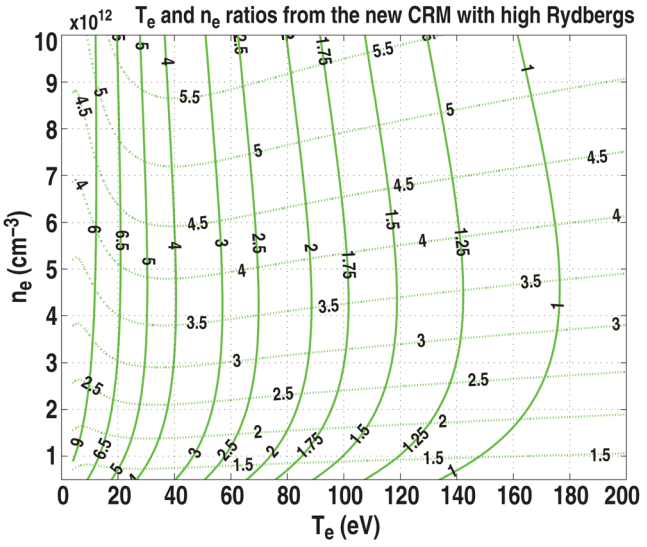

FIG. 3. (Color online) Modeled equilibrium solution with high Rydberg states included, for the electron temperature and density sensitive line ratios. Solid curve represents the calculated value for the 706.7 nm/728.3 nm electron temperature sensitive ratio; dotted curve represents the calculated value for the 667.9 nm/728.3 nm electron density sensitive ratio for our selected electron temperature and density mesh.

$$\frac{dn'_k}{dt} = \lambda_k n'_k + r'_k. \tag{18}$$

By knowing the initial conditions $n'_k(0)$ at $t=0$ from $\boldsymbol{n}'(0) = \boldsymbol{V}^{-1} \cdot \boldsymbol{n}(0)$, and by applying $\boldsymbol{r}' = \boldsymbol{V}^{-1} \cdot \boldsymbol{r}$, we obtain the time dependent solution for any kth-term transformed population in the form

$$n'_k(t) = \sum_{j=1}^{N} V^{-1}_{k,j} \left[\left(n_j(0) + \frac{r_j}{\lambda_k} \right) \exp(\lambda_k t) - \frac{r_j}{\lambda_k} \right]. \tag{19}$$

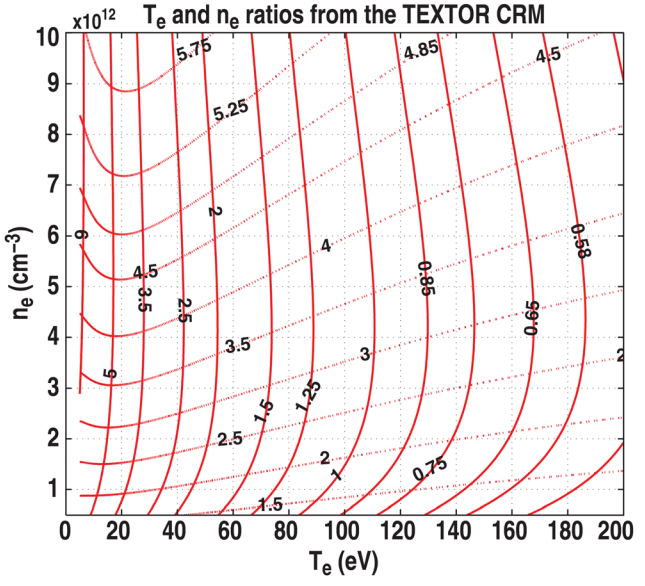

FIG. 4. (Color online) TEXTOR modeled equilibrium solution for the electron temperature and density sensitive line ratios. Solid curve represents the calculated value for the 706.7 nm/728.3 nm electron temperature sensitive ratio; dotted curve represents the calculated value for the 667.9 nm/728.3 nm electron density sensitive ratio.

We now apply the frame transformation $\boldsymbol{n}(t) = \boldsymbol{V} \cdot \boldsymbol{n}'(t)$ to get the final form of the time dependent solution for any of the ith-term populations, thus we obtain

$$n_i(t) = \sum_{k=1}^{N} V_{i,k} \left\{ \sum_{j=1}^{N} V^{-1}_{k,j} \left[\left(n_j(0) + \frac{r_j}{\lambda_k} \right) \exp(\lambda_k t) - \frac{r_j}{\lambda_k} \right] \right\}, \tag{20}$$

which could be applied for any set of electron density and temperature values at any given time t. We note that our solution also depends on the initial population values $\boldsymbol{n}(0)$; these values can be set as well since they depend on the initial population of the thermal beam. We use initial normalized values, thus the sum of all the populations at any given moment is constant (or equal to one). In our case (thermal helium beam), we assume our total initial population to be in the ground state $1s^2(^1S)$, therefore we set $n_1(0) = 1.0$ and $n_m(0) = 0.0$ for $m = 2 \ldots N$. In case of a high energy helium beam, the ground state $1s^2(^1S)$ may be 80% populated and the metastable $1s2s(^3S)$ 20%; this would give us initial population values of $n_1(0) = 0.8$, $n_2(0) = 0.2$, and $n_m(0) = 0.0$ for $m = 3 \ldots N$. In our approach, we compute our eigenvector matrix $\boldsymbol{V}$, its inverse $\boldsymbol{V}^{-1}$, the eigenvalue vector $\boldsymbol{\lambda}$, and the charge-exchange/recombination vector $\boldsymbol{r}$ as a function of a electron temperature T_e and density n_e $(N \times M)$ grid. This results in a $N_{Te} \times M_{ne}$ set of data which we simply store and use as needed by our analytic solution [Eq. (20)] in order to calculate our time dependent line ratio for a $N_{Te} \times M_{ne}$ grid for a specific time t, and an initial set of population values $\boldsymbol{n}(0)$. For our neutral beam, we do not have recombination and charge-exchange into our neutrals, therefore we eliminate the r_j term in Eq. (20), thus simplifying much further our time dependent solution to

$$n_i(t) = \sum_{k=1}^{N} V_{i,k} \sum_{j=1}^{N} V^{-1}_{k,j} n_j(0) \exp(\lambda_k t). \tag{21}$$

This simplification eliminates the need for calculating the charge-exchange/recombination vector $\boldsymbol{r}$ for the electron temperature-density grid. We note that even though our solution is simplified, the general solution [Eq. (20)] may still apply for the case of a high energy charged beam, in which recombination and charge-exchange would have to be included into the $\boldsymbol{r}$ vector. To compare our time dependent population solutions against the normalized equilibrium populations [Eq. (10)], we normalize our solutions with respect to the ground state (n_i/n_o) by again setting $n_1 = n^o = 1$. Thus, our normalized time dependent population solutions are simply expressed in the form $n_i(t)/n_1(t)$, with $i = 2 \ldots N$.

Figure 5 shows our equilibrium and time dependent population calculations for the $1s3s(^3S)$, $1s3s(^1S)$, and $1s3d(^1D)$ terms for the arbitrary values of $T_e = 15.0$ eV and $n_e = 1.0 \times 10^{12}\,\mathrm{cm}^{-3}$. These terms correspond to the 706.7 nm, 728.3 nm, and 667.9 nm emission line excited populations. Notice the large relaxation time differences between the metastable-based populated term (^3S) and the ground-based populated terms (^1S and ^1D) are of roughly 25 μs. By having an average thermal helium beam speed of

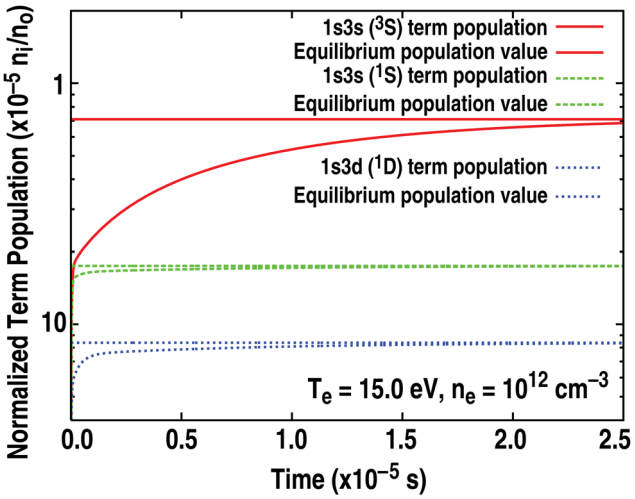

FIG. 5. (Color online) Time dependent term population solutions for the $1s3s(^3S)$, $1s3s(^1S)$, and $1s3d(^1D)$ normalized with respect to the ground state. Horizontal lines represent the modeled equilibrium values.

$v_b = 1500\,\text{m/s}$,[1] we obtain a value for the traveled distance of 3.75 cm before the metastable-based populated terms reach equilibrium for these electron temperature and density values. Such a large relaxation time must be accounted for when applying the line ratio diagnostic technique. This is our main motivation for pursuing a full time dependent solution for this diagnostic. Figure 6 shows the time dependent electron temperature sensitive $1s3s(^3S)/1s3s(^1S)$, electron density sensitive $1s3d(^1D)/1s3s(^1S)$, and electron temperature/density sensitive $1s3s(^3S)/1s3d(^1D)$ population ratio solutions for the same set of conditions. Notice that the density sensitive (singlet term ground-populated) line ratio reaches equilibrium almost immediately as expected; this shows that a time dependent approach is unnecessary for singlet-based populated terms, thus making the equilibrium solution a good approach for determining electron densities. On the other hand, we see that a time dependent solution for the

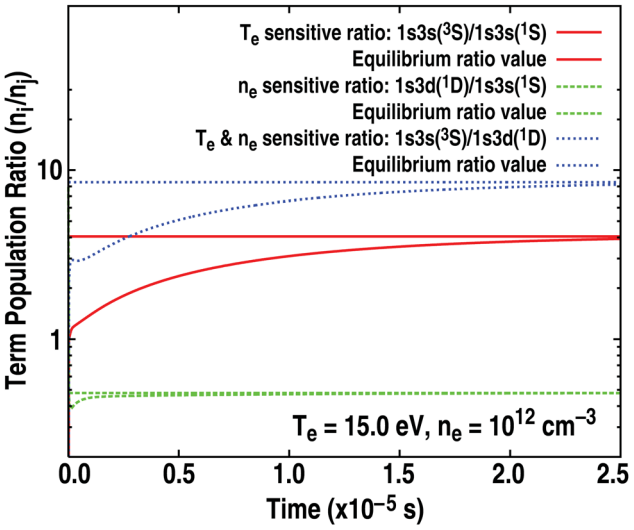

FIG. 6. (Color online) Time dependent solutions for the $1s3s(^3S)$, $1s3s(^1S)$, and $1s3d(^1D)$ term population ratios. Horizontal lines represent the modeled equilibrium values.

temperature sensitive (triplet term metastable-populated) line ratio solutions cannot be ignored and must be implemented. We also see how the population ratio is lower than the equilibrium ratio during the time progression when looking at the temperature sensitive equilibrium line ratio shown in Fig. 2. The lower the line ratio value is, the higher the predicted temperature value obtained. This is the reason why the equilibrium solution predicts unphysical high electron temperatures for part of the SOL-wall region where the temperatures and densities are not as high.

In order to implement this time dependent diagnostic, we start at an initial radial position r_o, where the helium thermal beam is first introduced into the vacuum chamber. By knowing the initial population values $\boldsymbol{n}(0)$, the initial radial position r_o, the radial position of the first experimental point r_1, and the average velocity of the thermal beam v_b, we obtain our relaxation time $t_1 = (r_o - r_1)/v_b$. From this value, we compute our populations $\boldsymbol{n}(t_1)$ for the time dependent electron temperature-density grid by means of Eq. (13), thus giving us the line ratios for $t = t_1$; $R_{Te}(t_1)$, $R_{ne}(t_1)$, and $R_{Te,ne}(t_1)$ as functions of electron temperature and density. We then obtain the set of local electron temperature and density values (T_{e_1}, n_{e_1}) for the first experimental point by means of Eq. (14). This way we get our new initial set of population values $\boldsymbol{n}^{\text{new}}(0) = \boldsymbol{n}(t_1, T_{e_1}, n_{e_1})$ that will be used for calculating our next set of experimental values. With this method, we obtain the solutions for any of the kth experimental points

$$t_k = \frac{|r_o - r_k|}{v_b} - t_{k-1},$$
$$\boldsymbol{n}^k(0) = \boldsymbol{n}^{k-1}(t_{k-1})(T_{e_{k-1}}, n_{e_{k-1}}). \tag{22}$$

Since the relaxation times are only significant for a set of low values of electron temperature and density, we do not need to calculate our quantities for the same large grid as we do in the equilibrium case. In order to quantify the limits of application of the time dependent model, we make use of the following minimization:

$$\varepsilon^2 = \sum_{i=1}^{N} \left[1 - \frac{n_i(t)}{n_i^{eq}}\right]^2, \tag{23}$$

where $n_i(t)$ is the time dependent population for any of the N terms for an specific set of electron temperature and density values, and n_i^{eq} is the equilibrium population. To estimate a value for our minimization factor ε^2, we use an exponential model as an approximation. Let us first assume that the time dependent solution for the populations is given by the approximate form

$$n_i(t) = n_i^{eq}[1 - \exp(-t/\tau)], \tag{24}$$

where τ is the relaxation time as a function of electron temperature and density, which would represent an exact solution if our system of equations [Eq. (3)] would be a uncoupled set. When $t = \tau$, the ratio of the time dependent population and the equilibrium populations give us

$n_i/n_i^{eq} \approx 0.632$. By plugging this value back into Eq. (23) and by setting $N = 19$ terms (as in the case of our CRM), we obtain a minimization factor of $\varepsilon^2 \approx 2.57$. By having obtained an estimation for the minimization factor, we choose a value of $\varepsilon^2 = 1.0$ to be applied into our analytical model [Eq. (21)], and thus obtain an average value for our relaxation time as function of electron temperature and density $\tau(T_e,n_e)$. When using $\varepsilon^2 = 1.0$ into our minimization equation [Eq. (23)], we obtain an average population ratio of $n_i/n_i^{eq} \approx 0.98$ for the singlet $1s3s(^1S)$ and $1s3d(^1D)$ terms and $n_i/n_i^{eq} \approx 0.71$ for the triplet $1s3s(^3S)$ term. Figure 7 shows our results for the population relaxation time of the ^3S metastable term of helium as a function of electron temperature and density. We notice that this relaxation time is much more sensitive to electron density than electron temperature variations. We see that for electron densities roughly higher than $1.0 \times 10^{12}\,\mathrm{cm}^{-3}$, the relaxation times are in the order of microseconds. Therefore for electron density values higher than our estimated threshold value of $1.0 \times 10^{12}\,\mathrm{cm}^{-3}$, we can apply with confidence the equilibrium model for our line ratio diagnostic. Therefore, we choose a smaller set of electron temperature and density values for computation of the eigenvector matrix $\boldsymbol{V}$, its inverse $\boldsymbol{V}^{-1}$, and the eigenvalue vector $\boldsymbol{\lambda}$ [Eq. (21)], thus reducing the size of these files. We use an electron temperature set from $T_e = 1$ to 125 eV with resolution of $\Delta T_e = 1\,\mathrm{eV}$, and four electron density sets from $n_e = 1.0 \times 10^8$ to $1.0 \times 10^9\,\mathrm{cm}^{-3}$ with resolution of $\Delta n_e = 1.0 \times 10^8\,\mathrm{cm}^{-3}$, and $n_e = 1.0 \times 10^9$ to $1.0 \times 10^{10}\,\mathrm{cm}^{-3}$ with resolution of $\Delta n_e = 1.0 \times 10^9\,\mathrm{cm}^{-3}$, and $n_e = 1.0 \times 10$ to $1.0 \times 10^{12}\,\mathrm{cm}^{-3}$ with resolution of $\Delta n_e = 1.0 \times 10^{10}\,\mathrm{cm}^{-3}$, and $n_e = 1.0 \times 10^{12}$ to $5.0 \times 10^{12}\,\mathrm{cm}^{-3}$ with resolution of $\Delta n_e = 1.0 \times 10^{11}\,\mathrm{cm}^{-3}$. We have chosen these ranges of electron densities since we expect the relaxation times of the ^3S metastable term to be significant as shown by Fig. 7. We do not expect to have electron densities lower than $10^8\,\mathrm{cm}^{-3}$, and we have also included some overlap in the higher limit of the electron density with respect to those chosen for our equilibrium solution.

V. ERROR PROPAGATION ANALYSIS

In order to quantify the range of confidence in our determined electron temperature and density values with respect to the uncertainty given by the line intensity measurements and our hybrid model, we apply a simple uncorrelated error propagation model. Unfortunately, we do not yet have the definite capability of propagating the uncertainties obtained from basic electron impact rate coefficients from the atomic data employed in our CRM for calculation of term populations. We do not have a way of evaluating the quality of the high Rydberg states either, but when calculating the three line ratios with and without high Rydberg effects included, we found average differences of 17.42%, 8.30%, and 10.40% lower values for the 706.7 nm/728.3 nm, 667.9 nm/728.3 nm, and 706.7 nm/667.9 nm modeled line ratios with high Rydberg effects to those without them. We do not include these differences in our error propagation analysis but we limit our comparisons to results

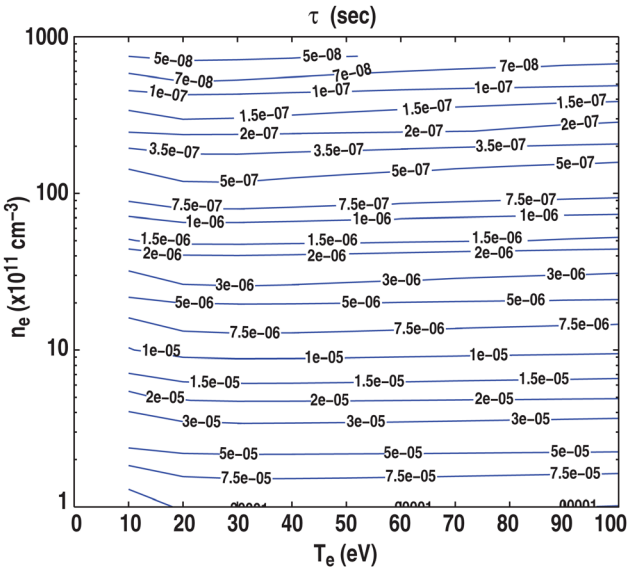

FIG. 7. (Color online) Modeled population relaxation time for the ^3S metastable term of helium as a function of electron temperature and density. Solid line represents the average relaxation time τ, as a function of electron temperature and density. We notice the high sensitivity on electron density in comparison to electron temperature.

obtained by experimental measurements of electron temperature and density values. However, we estimate a small contribution of the errors in the atomic data set to our population values by assuming that most of these contributions end up canceling due to high population correlation; this assumption will be discussed later in this section. For the helium line ratio diagnostic, we determine our electron temperature and density values and their uncertainties from the ratio of three different lines; these ratios are given by an electron temperature sensitive line ratio R_{Te}, an electron density sensitive line ratio R_{ne}, and an electron temperature and density sensitive line ratio $R_{Te,ne}$, determined experimentally from

$$R_{T_e}^{exp} = \frac{I^{(706.7\mathrm{nm})}}{I^{(728.3\mathrm{nm})}},$$
$$R_{n_e}^{exp} = \frac{I^{(667.9\mathrm{nm})}}{I^{(728.3\mathrm{nm})}}, \tag{25}$$
$$R_{T_e,n_e}^{exp} = \frac{I^{(706.7\mathrm{nm})}}{I^{(667.9\mathrm{nm})}}.$$

For any given experimental ratio $R_{ab}^{exp} = I^a/I^b$ with line intensities and experimental uncertainties: $I^a \pm \sigma_a$ and $I^b \pm \sigma_b$, the uncertainty of the ratio can be expressed by the simple uncorrelated error formula

$$\left(\frac{\sigma_{R_{ab}}^{exp}}{R_{ab}^{exp}}\right)^2 = \left(\frac{\sigma_a}{I^a}\right)^2 + \left(\frac{\sigma_b}{I^b}\right)^2, \tag{26}$$

which we use to solve for $\sigma_{R_{ab}}$, thus we get

$$\sigma_{R_{ab}}^{exp} = \pm R_{ab}^{exp}\sqrt{\left(\frac{\sigma_a}{I^a}\right)^2 + \left(\frac{\sigma_b}{I^b}\right)^2}. \tag{27}$$

To calculate our hybrid line ratio model, we have used the approximation given by Eq. (13). Table II shows the

TABLE II. NIST Einstein $A_{i\to j}$ coefficients.

Einstein coefficient[a]	Value (s^{-1})	Uncertainty $\left(\frac{\sigma_{A_{i\to j}}}{A_{i\to j}}\right)$
$A_{i\to j}^{667.9}$	6.37201×10^{7}	1.41421×10^{-2}
$A_{i\to j}^{706.7}$	2.78532×10^{7}	1.73205×10^{-2}
$A_{i\to j}^{728.3}$	1.82990×10^{7}	1.00000×10^{-2}

[a]Values obtained from NIST (Ref. 23).

Einstein coefficient values and their uncertainties used in our line ratio model.

From our calculated line ratio [Eq. (13)], we write our predicted uncertainty in the form

$$\sigma_R^{mod} = \pm R^{mod} \times \sqrt{\left(\frac{\sigma_{A_{i\to j}}}{A_{i\to j}}\right)^2 + \left(\frac{\sigma_{A_{k\to l}}}{A_{k\to l}}\right)^2 + \left(\frac{\sigma_{n_i}}{n_i}\right)^2 + \left(\frac{\sigma_{n_k}}{n_k}\right)^2 - 2\frac{\sigma_{n_i}\sigma_{n_k}}{n_i n_k}\gamma_{ik}}, \tag{28}$$

where σ_n are the uncertainties of the n populations, γ_{ik} is the population correlation coefficient, and σ_A/A are the uncertainty values for the Einstein coefficients (Table II). By assuming the relative errors $\sigma_{ni}/n_i \approx \sigma_{nk}/n_k = \sigma_n/n$ and $\gamma_{ik} = \gamma_n$, we rewrite Eq. (28) in the form

$$\sigma_R^{mod} \approx \pm R^{mod} \sqrt{\left(\frac{\sigma_{A_{i\to j}}}{A_{i\to j}}\right)^2 + \left(\frac{\sigma_{A_{k\to l}}}{A_{k\to l}}\right)^2 + 2\left(\frac{\sigma_n}{n}\right)^2 (1-\gamma_n)}. \tag{29}$$

From this equation [Eq. (29)], we see that for a correlation coefficient $\gamma_n \approx 1.0$, the contributions from the error populations end up vanishing. Even though we do not have a way to calculate these values yet, we expect a high level of correlation between the populations due to the coupled nature of the differential equations [Eq. (1)]. By using this approximation, we quantify these errors by assuming a correlation factor of $\gamma_n = 0.95$. For our model, we also guess relative error values of $\sigma_n/n = 0.05$ for the populations. Efforts are being conducted in order to propagate fundamental errors from collision cross-sections into rate coefficients and rate coefficients into populations. We expect to be able to obtain numerical values for the uncertainties in the populations and their correlation factors in the near future.

By having both the experimental and modeled uncertainty values, we write our total uncertainty quantities in the form

$$\sigma_R = \pm\sqrt{(\sigma_R^{exp})^2 + (\sigma_R^{mod})^2}. \tag{30}$$

We focus our discussion mainly on the electron temperature and electron density sensitive line ratios with their respective uncertainties $R_{T_e} \pm \sigma_{R_{T_e}}$ and $R_{n_e} \pm \sigma_{R_{n_e}}$ determined from Eq. (30). We notice from Fig. 2 that the electron temperature sensitive line ratio behaves almost uniformly with respect to electron density variations. In the same way, it shows that the electron density sensitive line ratio behaves almost uniformly with respect to electron temperature variations. In order to illustrate the expected uncertainty behavior in our electron temperature and density values $\pm\sigma_{Te}$ and $\pm\sigma_{ne}$, we focus our discussion on the electron temperature sensitive line ratio (Fig. 2) of $n_e = 1.0 \times 10^{12}\,cm^{-3}$ shown in Fig. 8 and an electron density sensitive line ratio (Fig. 2) of $T_e = 50\,eV$ shown in Fig. 9 as an example. Figure 8 shows that the predicted electron temperature values become more sensitive to line ratio uncertainties $(\pm\sigma_{R_{T_e}})$ for roughly $T_e > 100\,eV$ and less sensitive for lower electron temperatures. At $T_e > 100\,eV$, we obtain temperature variations roughly between 78 and 134 eV for our hypothetical temperature sensitive line ratio of $R \approx 1.76 \pm 0.35$ (Fig. 8); this represents an error in the line ratio of $\approx$20%.

For the case of the electron density diagnostic (Fig. 9), we obtain an opposite behavior. We notice that for a value of roughly $n_e > 5.0 \times 10^{11}\,cm^{-3}$, the predicted electron density values become less sensitive to line ratio uncertainties $(\pm\sigma_{R_{n_e}})$ than in the case of lower electron density values. Therefore, we can expect a good measure of confidence for the electron temperature diagnostic for $T_e < 100\,eV$ values and for the electron density diagnostic for $n_e > 5.0 \times 10^{11}\,cm^{-3}$. This analysis also shows the importance of reducing the experimental line emission uncertainties when applying the line ratio technique for the purpose of electron temperature and density diagnostic.

VI. HYBRID DIAGNOSTIC MODEL IMPLEMENTATION AND RESULTS

We implement the hybrid diagnostic technique approach by overlapping the electron temperature and density values obtained from the time dependent solution, with those obtained from the equilibrium solution. The maximum electron density value chosen for the time dependent solution is $5.0 \times 10^{12}\,cm^{-3}$. This does not mean it is necessary to apply the time dependent solution for all the cases where $n_e \le 5.0 \times 10^{12}\,cm^{-3}$, instead we have chosen the threshold value of $n_e < 1.0 \times 10^{12}\,cm^{-3}$ which we reserve exclusively for the time dependent model. After this minimum density

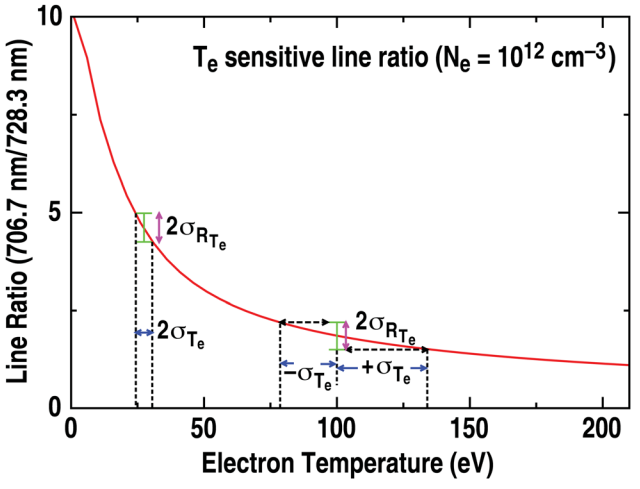

FIG. 8. (Color online) Modeled error propagation for the electron temperature sensitive line ratio.

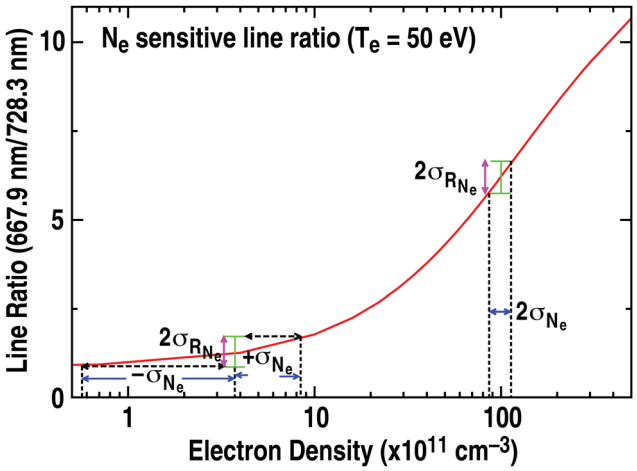

FIG. 9. (Color online) Modeled error propagation for the electron density sensitive line ratio.

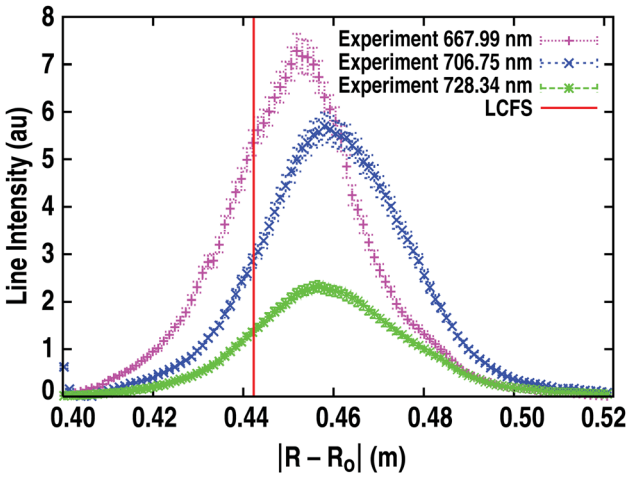

FIG. 10. (Color online) Experimental 667.9 nm, 706.7 nm, and 728.3 nm helium emission lines from shot number 101401 at TEXTOR.[1]

value is reached, we monitor the convergence of the two solutions by applying

$$\xi^2 = \left[1 - \frac{T_e(t)}{T_e^{eq}}\right]^2 + \left[1 - \frac{n_e(t)}{n_e^{eq}}\right]^2, \tag{31}$$

where $T_e(t)$ and $n_e(t)$ are the electron temperature and density values determined from the time dependent model, while T_e^{eq} and n_e^{eq} are those determined from the equilibrium model. Since the time dependency affects mainly the triplet spin system ^3S, we expect higher differences for the electron temperatures, while we expect a faster level of convergence for the electron densities. After the threshold value of $1.0 \times 10^{12}\,\mathrm{cm}^{-3}$ is reached by the time dependent solution, we monitor the ξ^2 quantity till it hits its minimum, then the electron temperature and density values are determined exclusively by the equilibrium solution.

For the purpose of testing our hybrid diagnostic model, we make use of available experimental helium emission data from the low field side thermal beam system for four different L-mode shots from TEXTOR.[1] The TEXTOR tokamak has a major radius of $R_o = 1.75\,\mathrm{m}$, a minor radius of $a = 0.46\,\mathrm{m}$, and a dynamic ergodic divertor (DED or limiter). The thermal beam has a Gaussian distributed mean velocity of $v_{mean} \approx 1.4-1.6\,\mathrm{km/s}$ depending on the nozzle temperature and a divergence angle of 20°.[1] For our time dependent diagnostic purposes, we have chosen an average thermal beam velocity value of $v_b = 1.5\,\mathrm{km/s}$. In the TEXTOR experimental settings, the gas is introduced into the vacuum chamber at $r_o = |R - R_o| = 0.554\,\mathrm{m}$,[1] where it propagates radially from the wall into the SOL and part of the edge region after crossing the last closed flux surface (LCFS). By applying both the time dependent and equilibrium line ratio diagnostic models, we determine a set of experimental electron temperatures $T_e(r)$ and densities $n_e(r)$ along the radial direction $|R - R_o|$ of the vacuum chamber. Figure 10 shows experimental helium emission intensities for the 667.9, 706.7, and 728.3 nm helium lines from shot #101401. We have analyzed similar data sets for shots #102175, #102118, and #101738 from TEXTOR.[1] Table III shows the characteristics of these specific TEXTOR shots.[1] From these experimental sets, we determine electron temperature and density profiles for both the time dependent solution and equilibrium solution models. We are also showing the results of the contributions from both techniques to the hybrid model. We analyze the predicted results for electron temperature and density profiles from both models with and without high Rydberg states and compare them against different diagnostic data for the four different shots. We compare our predictions against the equilibrium (stationary) helium line ratio solution applied routinely at TEXTOR. We also compare our results against edge Thomson and Li beam data for shot 101401 (Figs. 11 and 12).

Figure 11 shows the electron temperature predictions for shot #101401 by employing both models with and without high Rydberg states. We notice a high level of agreement when comparing the results of the hybrid model without high Rydbergs against the edge Thomson data from TEXTOR; we also see relatively good agreement by using the model with high Rydberg states. We find as well the unphysical high temperature values predicted by the equilibrium model when approaching the SOL-wall region for not taking into account the relaxation times of the triplet spin system. In contrast, both time dependent models with and without high Rydbergs predict more reasonable values for the temperatures when comparing against the Thomson data. The time dependent equilibrium solution has the tendency to converge with the equilibrium solution (as expected) when approaching a higher electron density region (into the plasma). We obtain better agreement with Thomson electron

TABLE III. TEXTOR discharges overview (Ref. 1).

Discharge number	Heating method	n_e ($10^{13}\,\mathrm{cm}^{-3}$)	I_P (kA)	B_T (T)	R_c (m)	P_H (kW)
101401	NBI	3.3	370	1.9	1.735	850
102175	NBI	2.5	255	1.3	1.755	2400
102118	NBI	3.6	355	2.3	1.755	1200
101738	Ohmic	3.1	355	2.3	1.755	300

temperatures for the equilibrium solution without high Rydbergs at the SOL-edge region where the time dependent solution is no longer necessary. When looking at the model with high Rydbergs included, we find electron temperature values 21.14% lower than the model without high Rydbergs. Both models predict closer electron temperature values to the Thomson data than the TEXTOR equilibrium model. We obtain an average of 40 eV differences between our model without high Rydbergs and the equilibrium (stationary) solution applied routinely at TEXTOR.

Figure 11 shows the electron density predictions for the same shot. We notice that both the time dependent and equilibrium solutions converge very quickly at the low field region in comparison to the electron temperature predictions (Fig. 11). This is expected since the relaxation times of the singlet spin system are too short to cause any major differences. We obtain good agreement between both of our hybrid models, Li beam, and the TEXTOR equilibrium model at the low field region. We find some disagreement between all these models and the Thomson density data. Note that there is a systematically 10%–20% lower than measured with the helium line ratio technique. The density evaluation from the Thomson light relies on Raleigh calibration which is done frequently at TEXTOR, and the uncertainty from this calibration is contained in the error bars for the Thomson data points. However, as shown in Figs. 13 and 14 of Ref. 1 (O. Schmitz *et al.*), this deviation between Thomson and the helium beam data depends on the actual discharge conditions. When approaching the high field region, we see differences between the Thomson data and the predictions from both new models with and without high Rydberg states as well as the equilibrium TEXTOR predictions. We find that the new equilibrium model without high Rydbergs predicts closer density values to the Thomson data than the values predicted from the TEXTOR equilibrium model. In the other hand, our new equilibrium model with high Rydberg states included predicts on average electron density values 16.0% higher than those from the new model without high Rydbergs states. These values

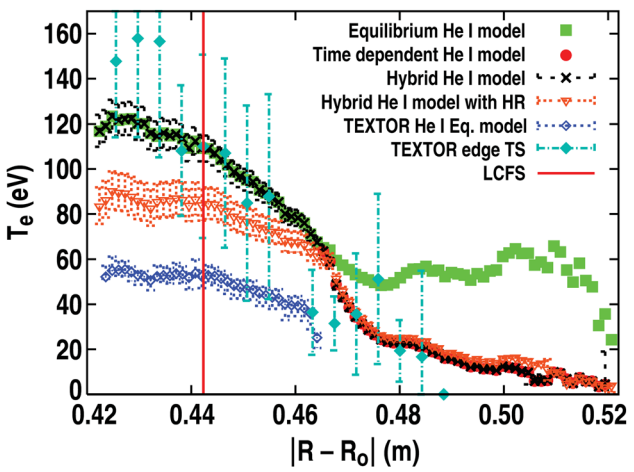

FIG. 11. (Color online) Electron temperature profiles determined from the hybrid helium line ratio for both models with and without high Rydbergs included, along the radial direction of the vacuum chamber for shot number 101401 at TEXTOR.[1]

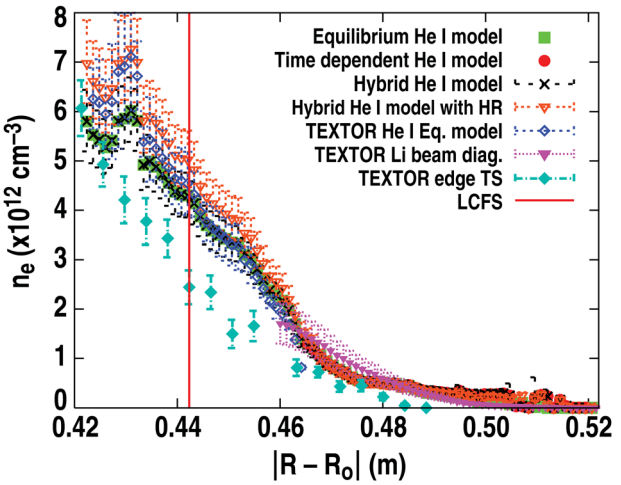

FIG. 12. (Color online) Electron density profiles determined from the hybrid helium line ratio for both models with and without high Rydbergs included, along the radial direction of the vacuum chamber for shot number 101401 at TEXTOR.[1]

are higher than the equilibrium TEXTOR model as well, but at the same time, these three models are within the error bars of each other.

Overall, a direct comparison can be made between the new equilibrium model without high Rydbergs and the equilibrium TEXTOR model (which does not include high Rydbergs either). Muñoz Burgos *et al.*[22] have shown that these differences are mainly caused by the differences in the atomic datasets employed in our model and the one in TEXTOR, and from looking at the comparison between the newly calculated rate coefficients against atomic experimental data,[17] it becomes clear that we should expect better agreement when applying the newly calculated RMPS data.

When analyzing the new model with high Rydberg states included, we find that it gives closer results to the Thomson data for the electron temperature values than those from the TEXTOR equilibrium solution. In the other hand, the TEXTOR equilibrium model gives closer electron density values to the Thomson data than those from the new model with high Rydberg states included. In general, both of the new models (with and without high Rydberg states) give closer results when compared to the Thomson electron temperature data than the TEXTOR model, and it seems that the new model without high Rydberg states included gives the closest agreement with the Thomson data.

There is not a experimental way to measure directly the effects of high Rydberg states into the populations; our term-resolved low n-shell atomic data are supplemented with data for the higher n-shells up to $n = 500$. We suspect that such a high n-shell number may be physically impossible due to higher density effects similar to those causing the Balmer jump observed in astrophysical plasmas,[28] where it is shown that the highest n-shell values are limited by the density. This could explain the higher level of agreement seeing between both with and without high Rydbergs models in the lower density region for electron temperatures and densities, and then both diverging slowly as approaching the higher electron density region (high field). Another possibility is

that the atomic data included in the projection matrix, specially the ECIP approximation method[26] employed in the high Rydberg ionization rate coefficient calculations may overestimate the amount of ionization in our high n-shell model. Further study and experimental data are necessary in order to make a definite conclusion. Some other source of errors may have occurred by our assumption of a uniform line of sight profile applied in our line ratio model [Eq. (12)], since at larger distances from the nozzle (high field region), the expansion of the beam becomes significantly wide, and integration along the line of sight must be taken into account in our calculations.

VII. CONCLUSIONS

We have successfully developed a hybrid time dependent/independent helium line ratio diagnostic that overcomes the problem of long relaxation times for the metastable based terms. This method has allowed us to increase the radial range of diagnostic application when compared against the current equilibrium helium line ratio model used at TEXTOR.[1] These capabilities are limited to regions where the electron temperature and density profiles are roughly uniform in order to avoid integration along the line of sight. For non-uniform/non-localized sources, we cannot expect our model to be as accurate since predictions are going to represent an average value of the electron temperatures and densities along the line of sight instead of a local value. It has been shown that including the line of sight for line emission modeling may play an important role when applying the line ratio diagnostic technique.[29] We have also compared the results against a model that includes high Rydberg effects into the collisional radiative model; we found better experimental agreement with the simpler model that does not include these effects. Further experimental evidence is needed in order to assess the effects of including high Rydberg effects into collisional radiative calculations.

ACKNOWLEDGMENTS

This work was supported in part by the US Department of Energy under DE-AC05-06OR23100 and DE-FC02-04ER54698. The authors wish to acknowledge the support of the atomic physics group at Auburn University, the ADAS consortium, the support of Yuhong Xu for his work in the TEXTOR fast probe data, Mikhael Kantor for the TEXTOR edge Thomson data contribution, and Nicolas Commaux for his help preparing some of the figures.

[1]O. Schmitz, I. L. Beigman, L. A. Vainshtein, B. Schweer, M. Kantor, A. Pospieszczyk, Y. Xu, M. Krychowlak, M. Lehnen, U. Samm, B. Unterberg, and the TEXTOR Team, Plasma Phys. Controlled Fusion **50**, 115004 (2008).
[2]A. Pospieszczyk, G. Chevalier, Y. Hirooka, R. W. Conn, R. Doerner, and L. Schmitz, Nucl. Instum. Methods Phys. Res. **B72**, 207 (1992).
[3]Y. Andrew and M. G. O'Mullane, Plasma Phys. Controlled. Fusion **42**, 301 (2000).
[4]H. Kubo, M. Goto, H. Takenaga, A. Kumagai, T. Sugie, S. Sakurai, N. Asakura, S. Higashijima, and A. Sakasai, J. Plasma Fusion Res. **75**, 945 (1999).
[5]J. W. Ahn, D. Craig, G. Fiksel, D. J. Den Hartog, J. K. Anderson, and M. G. O'Mullane, Rev. Sci. Instrum. **77**, 10F114 (2006).
[6]A. R. Field, P. G. Carolan, N. J. Conway, and M. G. O'Mullane, Rev. Sci. Instrum. **70**(1), 355 (1999).
[7]R. J. Maqueda, G. A. Wurden, S. Zweben, L. Roquemore, H. Kugel, D. Johnson, S. Kaye, S. Sabbagh, and R. Maingi, Rev. Sci. Instrum. **72**(1), 931 (2001).
[8]S. Lisgo, P. Börner, G. F. Counsell, J. Dowling, A. Kirk, R. Scannell, M. G. O'Mullane, D. Reiter, and The MAST Team, J. Nucl. Mater. **390–391**, 1078 (2009).
[9]F. B. Rosmej, R. Stamm, S. Fritzsche, H. Capes, M. Koubiti, Y. Marandet, V. S. Lisitsa, N. Ohno, S. Takamura, and D. Nishijima, J. Nucl. Mater. **337–339**, 1101 (2005).
[10]N. K. Podder, J. A. Johnson III, C. T. Raynor, S. D. Loch, C. P. Ballance, and M. S. Pindzola, Phys. Plasmas **11**, 12 (2004).
[11]D. R. Bates, A. E. Kinston, and R. W. McWhirter, Proc. R. Soc. London, Ser. A **267**, 297 (1962).
[12]P. G. Burke and K. A. Berrington, *Atomic and Molecular Processes: An R-Matrix Approach* (Institute of Publishing (IOP), Bristol, 1993).
[13]K. Bartschat, Comput. Phys. Commun. **114**, 168 (1998).
[14]I. Bray and A. T. Stelbovics, Phys. Rev. A **46**, 69 (1992).
[15]D. V. Fursa and I. Bray, Phys. Rev. A **52**, 1279 (1995).
[16]A. Okamoto, K. Iwazaki, T. Isono, T. kobuchi, S. Kitajima, and M. Sasao, Plasma Fusion Res. **3**, 059 (2008).
[17]C. P. Ballance, D. C. Griffin, S. D. Loch, R. F. Boivin, and M. S. Pindzola, Phys. Rev. A **74**, 012719 (2006).
[18]S. D. Loch, C. P. Ballance, M. S. Pindzola, and D. P. Stotler, Plasma Phys, Controlled Fusion **51**, 105006 (2009).
[19]See http://www.adas.ac.uk for ADAS-Atomic Data and Analysis Structure.
[20]H. P. Summers, W. J. Dickson, M. G. O'Mullane, N. R. Badnell, A. D. Whiteford, D. H. Brooks, J. Lang, S. D. Loch, and D. C. Griffin, Plasma Phys. Controlled Fusion **48**, 263 (2006).
[21]N. R. Badnell, M. G. O'Mullane, H. P. Summers, Z. Altun, M. A. Bautista, J. Colgan, T. W. Gorczyca, D. M. Mitnik, M. S. Pindzola, and O. Zatsarinny, Astron. Astrophys. **406**, 1151 (2003).
[22]J. M. Muñoz Burgos, O. Schmitz, E. A. Unterberg, S. D. Loch, and C. P. Ballance, J. Nucl. Mater. **415**, S1155 (2011).
[23]See http://www.nist.gov/pml/data/asd.cfm for NIST Atomic Spectra Database.
[24]Y. Ralcheenko, At. Data Nucl. Data Tables **94**, 603 (2008).
[25]A. Burgess and J. A. Tully, Astron. Astrophys. **254**, 436 (1992).
[26]A. Burgess and H. P. Summers, Mon. Not. R. Astron. Soc. **174**, 345 (1976).
[27]R. D. Cowan, *The Theory of Atomic Structure and Spectra* (University of California Press, Berkeley, CA, 1981).
[28]J. Tennyson, *Astronomical Spectroscopy: An Introduction to the Atomic and Molecular Physics of Astronomical Spectra* (Imperial College Press, University College London, UK, 2005).
[29]J. M. Muñoz Burgos, Ph.D. thesis (Auburn University, Auburn, AL, 2009).